# The coupling interaction of a piezoelectric screw dislocation with a bimaterial containing a circular inclusion

**Hui Chai**
*School of Aeronautic Science and Engineering, Beihang University, Beijing, China*

**Chiping Jiang**
*School of Aeronautic Science and Engineering, Beihang University, Beijing, China*

**Fan Song**
*State Key Laboratory of Nonlinear Mechanics (LNM), Institute of Mechanics, Chinese Academy of Sciences, Beijing, China*

**Peng Yan**
*School of Aeronautic Science and Engineering, Beihang University, Beijing, China*

**Abstract**
The coupling interaction of a piezoelectric screw dislocation with a bimaterial containing a circular inclusion is investigated by the complex potential method and conformal mapping technique. Explicit series solutions are obtained and then cast into new expressions with the coupling interaction effects separated. The new expressions converge much more rapidly and their one-order approximation formulae have satisfactory accuracy in many cases. According to the generalized Peach–Koehler formula, the image force acting on the screw dislocation is explicitly obtained and numerically studied to reveal the coupling interaction arising from multiple material properties as well as the geometry of inhomogeneous phases. In all regions, the coupling interaction has a significant influence on the number, location and stability of dislocation equilibrium points. In particular, the inclusion can reverse the image force within a region in the material on the other side of the interface.

## 1. Introduction

The movement of dislocations in the materials can determine the strength of materials, how they will deform under a load and how they accommodate strain [1]. The investigation of dislocations interacting with inhomogeneities plays a fundamental and significant role in understanding material defects and

**Corresponding author:**
Fan Song, State Key Laboratory of Nonlinear Mechanics (LNM), Institute of Mechanics, Chinese Academy of Sciences, Beijing 100190, China.
Email: songfan.imech@gmail.com

thereby provides valuable insight into the strengthening and deformation mechanism of many heterogeneous elastic materials. In view of its importance, a number of contributions have been made on this problem during the last several decades since the earliest research by Head [2]. References [3–20] are some examples of contributions in this area.

Due to the capability of the conversion between mechanical and electric fields, piezoelectric materials are widely used to design actuators, sensors and other electronic products. In practical applications, it is found that material defects, such as dislocations, cracks, cavities and inclusions, can adversely influence the performance of such piezoelectric devices. In order to predict the performance and integrity of devices, the study on the interaction effect between piezoelectric dislocations and inhomogeneities has become an important and active topic recently. Pak [21] first derived the formula for computing the force on a piezoelectric dislocation in a piezoelectric material, and analyzed the interaction effect between a piezoelectric screw dislocation and a traction-charge-free boundary. After that, the studies mainly focused on the interaction of a piezoelectric dislocation with different shapes of inhomogeneities (such as bimaterial interface [22], circular [23] or elliptical [24–26] inhomogeneities and cracks [27]) and various properties of interfaces (such as the perfectly bonded interface [22–26], interphase layer [28,29], interfacial crack [30,31], imperfect interface [32] and viscoelastic interface [33]).

There often are third-phase inclusions near a piezoelectric bimaterial interface, and thereby a strong coupling interaction appears. The coupling interaction arises from multiple material properties (mechanical, piezoelectric and dielectric properties), as well as from multiple inhomogeneous phases. It is crucial for understanding the interaction of piezoelectric dislocations with multiple inhomogeneities. However, this coupling interaction cannot be obtained by a linear superposition of existing solutions for an isolated inclusion and for a bimaterial interface. A basic understanding of such coupling interaction must be gained to achieve the full potential of piezoelectric composites and to design novel piezoelectric materials and structures.

This work deals with the coupling interaction of a piezoelectric screw dislocation with a bimaterial containing a circular inclusion by using the complex potential and conformal mapping technique. The emphasis is focused on the derivation of analytical solutions with coupling interaction effects separated and on the revelation of intricate coupling interaction phenomena.

## 2. Model and basic equations

Consider an infinite bimaterial containing a circular inclusion, as shown in Figure 1(a), where $S_1$, $S_2$ and $S_3$ denote three regions occupied by Material 1, Material 2 and the inclusion (with the radius $R_1$), respectively. $\Gamma_1$ and $\Gamma_2$ represent two perfectly bonded interfaces and $h$ is their distance. All the materials in the three regions are assumed to be transversely isotropic piezoelectric media. The origin of a Cartesian coordinate system lies at the center of the inclusion and the $x$-axis is perpendicular to the interface $\Gamma_1$. A generalized screw dislocation $b = \{b_w, \ b_\phi\}^{\mathrm{T}}$ [21,25], which is assumed to be straight and infinitely along the $z$-direction suffering a finite discontinuity in the displacement and electric potential
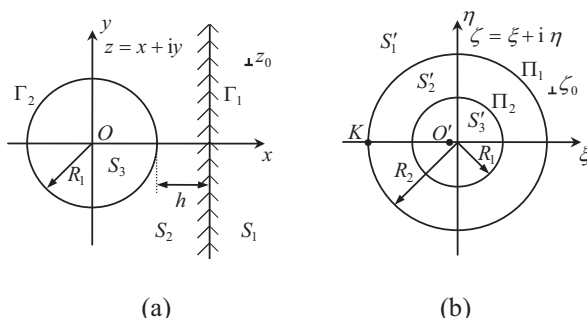


**Figure 1.** Conformal mapping: (a) a piezoelectric screw dislocation inside a bimaterial containing a circular inclusion in the z-plane; (b) mapping regions and characteristic points in the ζ-plane.

across the slip plane, is located at an arbitrary point $z_0$ in Material 1 ($S_1$), Material 2 ($S_2$) or the inclusion ($S_3$) ($z_0$ is plotted in Material 1 in Figure 1(a)).

For the problem under consideration, the anti-plane displacement $w$, stresses $\tau_{zx}$ and $\tau_{zy}$, electric potential $\phi$, and electric displacement components $D_x$ and $D_y$ in the Cartesian coordinates are only functions of $x$ and $y$, and they satisfy the following basic equations.

The equilibrium equation and charge equation:

$$\tau_{zx,x} + \tau_{zy,y} = 0 \text{ and } D_{x,x} + D_{y,y} = 0 \tag{1}$$

The mechanical and electric coupled constitutive relations [34]:

$$\left\{ \begin{matrix} \tau_{zx} \\ D_x \end{matrix} \right\} = \begin{bmatrix} c_{44} & e_{15} \\ e_{15} & -\varepsilon_{11} \end{bmatrix} \left\{ \begin{matrix} w_{,x} \\ \phi_{,x} \end{matrix} \right\} = M \left\{ \begin{matrix} w_{,x} \\ \phi_{,x} \end{matrix} \right\} \tag{2}$$

$$\left\{ \begin{matrix} \tau_{zy} \\ D_y \end{matrix} \right\} = \begin{bmatrix} c_{44} & e_{15} \\ e_{15} & -\varepsilon_{11} \end{bmatrix} \left\{ \begin{matrix} w_{,y} \\ \phi_{,y} \end{matrix} \right\} = M \left\{ \begin{matrix} w_{,y} \\ \phi_{,y} \end{matrix} \right\} \tag{3}$$

where $c_{44}$ is the longitudinal shear modulus at a constant electric field, $\varepsilon_{11}$ is the dielectric modulus at a constant stress field and $e_{15}$ is the piezoelectric modulus.

In order to facilitate the analysis, we introduce a generalized displacement vector $U = \{w, \phi\}^T$, two generalized stress vectors $\Sigma_x = \{\tau_{zx}, D_x\}^T$ and $\Sigma_y = \{\tau_{zy}, D_y\}^T$, and a generalized resultant force $T$ along any arc $AB$ in the piezoelectric material. Referring to the work by Liu et al. [28], these generalized vectors can be expressed by an analytical function vector $f(z) = \{f_w(z), f_\phi(z)\}^T$ ($z = x + iy$ is the complex variable):

$$U = \text{Re} \, f(z) \tag{4}$$

$$\Sigma_x - i\Sigma_y = Mf'(z) \tag{5}$$

$$T = \int_A^B \Sigma_n \mathrm{d}s = \int_A^B (\Sigma_x \mathrm{d}y - \Sigma_y \mathrm{d}x) = M \, \text{Im}[f(z)]_A^B \tag{6}$$

where $f_w(z)$ and $f_\phi(z)$ are conventional complex potentials, Re and Im, respectively, denote the real and imaginary part of the complex potential, the superscript prime denotes the differentiation with respect to the argument, $\Sigma_n$ is the normal component of generalized stresses on any arc $AB$ and $[\bullet]_A^B$ signifies the change in the bracketed function in going from the point $A$ to the point $B$ along any arc $AB$ (not passing through the interfaces).

The assumption of perfect bonding between dissimilar materials implies the continuity of generalized displacements and the normal component of stresses on two interfaces. Noting Equation (6), the continuity conditions can be expressed as

$$U_1 = U_2 \quad T_1 = T_2 \text{ on } \Gamma_1 \tag{7}$$

$$U_2 = U_3 \quad T_2 = T_3 \text{ on } \Gamma_2 \tag{8}$$

where the subscripts 1, 2 and 3 denote the three regions $S_1$, $S_2$ and $S_3$, respectively,

## 3. Solution

### 3.1. Conformal mapping and analytic continuation

To solve the problem, the following conformal mapping is introduced:

$$z = m(\zeta) = \frac{R_2\zeta + R_1^2}{\zeta + R_2} \tag{9}$$

where

$$\zeta = \xi + i\eta, \quad R_2 = (R_1 + h) + \sqrt{(R_1 + h)^2 - R_1^2} \tag{10}$$

The regions $S_1$, $S_2$ and $S_3$ in the $z$-plane (Figure 1(a)) are, respectively, mapped onto the regions $S_1'$ ($|\zeta| > R_2$), $S_2'$ ($R_1 < |\zeta| < R_2$) and $S_3'$ ($|\zeta| < R_1$) in the $\zeta$-plane (Figure 1(b)). The interfaces $\Gamma_1$ and $\Gamma_2$ are mapped onto the concentric circles $\Pi_1$ and $\Pi_2$, respectively. The coordinate origin $O$, the infinity and the point $z_0$ are mapped onto the points $O'(\zeta = -R_1^2/R_2)$, $K$ ($\zeta = -R_2$) and $\zeta_0$, respectively. The radii of $\Gamma_1$ and $\Pi_1$ both are $R_1$. The inverse transformation of Equation (9) is

$$\zeta = m^{-1}(z) = \frac{R_1^2 - R_2 z}{z - R_2} \tag{11}$$

According to the transformation rule of the compound function, the relationship between complex potentials in the two planes is

$$\boldsymbol{f}(z) = \boldsymbol{f}[m(\zeta)] = \boldsymbol{\varphi}(\zeta) \tag{12}$$

In the $\zeta$-plane, Equations (4)–(6), respectively, become

$$\boldsymbol{U} = \mathrm{Re}\,\boldsymbol{\varphi}(\zeta) \tag{13}$$

$$\boldsymbol{\Sigma}_x - i\boldsymbol{\Sigma}_y = \boldsymbol{M}\frac{\boldsymbol{\varphi}'(\zeta)}{m'(\zeta)} \tag{14}$$

$$\boldsymbol{T} = \boldsymbol{M}\,\mathrm{Im}[\boldsymbol{\varphi}(\zeta)]_A^B \tag{15}$$

Let $\boldsymbol{\varphi}_i(\zeta)$ ($i = 1$, 2 and 3) denote the complex potential within the corresponding region. In terms of the Schwarz Symmetry Principle, the following new complex potentials are introduced:

$$\boldsymbol{\varphi}_{1*}(\zeta) = -\bar{\boldsymbol{\varphi}}_1(R_2^2/\zeta) \text{ for } |\zeta| < R_2 \tag{16}$$

$$\boldsymbol{\varphi}_{2*}(\zeta) = -\bar{\boldsymbol{\varphi}}_2(R_2^2/\zeta) \text{ for } R_2 < |\zeta| < R_2^2/R_1 \tag{17}$$

$$\boldsymbol{\varphi}_{2**}(\zeta) = -\bar{\boldsymbol{\varphi}}_2(R_1^2/\zeta) \text{ for } R_1^2/R_2 < |\zeta| < R_1 \tag{18}$$

$$\boldsymbol{\varphi}_{3*}(\zeta) = -\bar{\boldsymbol{\varphi}}_3(R_1^2/\zeta) \text{ for } |\zeta| > R_1 \tag{19}$$

where the overbar represents the complex conjugate. Substituting Equations (13) and (15) into the continuity conditions (7) and (8), and noting Equations (16)–(19) and $t \cdot \bar{t} = |t|^2$ on $\Pi_1$ and $\Pi_2$ ($t$ is the point on the interfaces), the following complex potential vector equations in the $\zeta$-plane can be obtained:

$$\begin{cases} [\boldsymbol{\varphi}_1(t) + \boldsymbol{\varphi}_{2*}(t) + \boldsymbol{\varphi}_{3*}(t)]_{S_1'} = [\boldsymbol{\varphi}_{1*}(t) + \boldsymbol{\varphi}_2(t) + \boldsymbol{\varphi}_3(t)]_{S_2'} & |t| = R_2 \\ [\boldsymbol{\varphi}_{1*}(t) + \boldsymbol{\varphi}_2(t) + \boldsymbol{\varphi}_3(t)]_{S_2'} = [\boldsymbol{\varphi}_{1*}(t) + \boldsymbol{\varphi}_{2**}(t) + \boldsymbol{\varphi}_3(t)]_{S_3'} & |t| = R_1 \end{cases} \tag{20}$$

$$\begin{cases} [\boldsymbol{M}_2\boldsymbol{\varphi}_{2*}(t) - \boldsymbol{M}_1\boldsymbol{\varphi}_1(t) + \boldsymbol{M}_3\boldsymbol{\varphi}_{3*}(t)]_{S_1'} = [\boldsymbol{M}_1\boldsymbol{\varphi}_{1*}(t) - \boldsymbol{M}_2\boldsymbol{\varphi}_2(t) + \boldsymbol{M}_3\boldsymbol{\varphi}_3(t)]_{S_2'} & |t| = R_2 \\ [\boldsymbol{M}_1\boldsymbol{\varphi}_{1*}(t) - \boldsymbol{M}_2\boldsymbol{\varphi}_2(t) + \boldsymbol{M}_3\boldsymbol{\varphi}_3(t)]_{S_2'} = [\boldsymbol{M}_1\boldsymbol{\varphi}_{1*}(t) + \boldsymbol{M}_2\boldsymbol{\varphi}_{2**}(t) - \boldsymbol{M}_3\boldsymbol{\varphi}_3(t)]_{S_3'} & |t| = R_1 \end{cases} \tag{21}$$

where the subscripts $S_1'$, $S_2'$ and $S_3'$ refer to the function values as approached from the three corresponding regions, respectively. Equation (20) implies that $[\boldsymbol{\varphi}_1(\zeta) + \boldsymbol{\varphi}_{2**}(\zeta) + \boldsymbol{\varphi}_{3*}(\zeta)]$, $[\boldsymbol{\varphi}_{1*}(\zeta) + \boldsymbol{\varphi}_2(\zeta) + \boldsymbol{\varphi}_{3*}(\zeta)]$

and $[\boldsymbol{\varphi}_{1*}(\zeta) + \boldsymbol{\varphi}_{2*}(\zeta) + \boldsymbol{\varphi}_3(\zeta)]$ are the mutual direct analytical continuation and they can be expressed by a continuous function vector $\boldsymbol{\Psi}_U(\zeta)$:

$$\boldsymbol{\Psi}_U(\zeta) = \begin{cases} \boldsymbol{\varphi}_{1*}(\zeta) + \boldsymbol{\varphi}_{2**}(\zeta) + \boldsymbol{\varphi}_3(\zeta) & R_1^2/R_2 < |\zeta| < R_1 \\ \boldsymbol{\varphi}_{1*}(\zeta) + \boldsymbol{\varphi}_2(\zeta) + \boldsymbol{\varphi}_{3*}(\zeta) & R_1 < |\zeta| < R_2 \\ \boldsymbol{\varphi}_1(\zeta) + \boldsymbol{\varphi}_{2*}(\zeta) + \boldsymbol{\varphi}_{3*}(\zeta) & R_2 < |\zeta| < R_2^2/R_1 \end{cases} \tag{22}$$

Similarly, one can obtain another function vector $\boldsymbol{\Psi}_T(\zeta)$ from Equation (21):

$$\boldsymbol{\Psi}_T(\zeta) = \begin{cases} \boldsymbol{M}_1\boldsymbol{\varphi}_{1*}(\zeta) + \boldsymbol{M}_2\boldsymbol{\varphi}_{2**}(\zeta) - \boldsymbol{M}_3\boldsymbol{\varphi}_3(\zeta) & R_1^2/R_2 < |\zeta| < R_1 \\ \boldsymbol{M}_1\boldsymbol{\varphi}_{1*}(\zeta) - \boldsymbol{M}_2\boldsymbol{\varphi}_2(\zeta) + \boldsymbol{M}_3\boldsymbol{\varphi}_{3*}(\zeta) & R_1 < |\zeta| < R_2 \\ \boldsymbol{M}_2\boldsymbol{\varphi}_{2*}(\zeta) - \boldsymbol{M}_1\boldsymbol{\varphi}_1(\zeta) + \boldsymbol{M}_3\boldsymbol{\varphi}_{3*}(\zeta) & R_2 < |\zeta| < R_2^2/R_1 \end{cases} \tag{23}$$

Define

$$\boldsymbol{\Psi}_U(\zeta) = \begin{cases} \boldsymbol{\varphi}_{1*}(\zeta) + \boldsymbol{\varphi}_3(\zeta) & |\zeta| < R_1^2/R_2 \\ \boldsymbol{\varphi}_1(\zeta) + \boldsymbol{\varphi}_{3*}(\zeta) & |\zeta| > R_2^2/R_1 \end{cases} \tag{24}$$

and

$$\boldsymbol{\Psi}_T(\zeta) = \begin{cases} \boldsymbol{M}_1\boldsymbol{\varphi}_{1*}(\zeta) - \boldsymbol{M}_3\boldsymbol{\varphi}_3(\zeta) & |\zeta| < R_1^2/R_2 \\ \boldsymbol{M}_3\boldsymbol{\varphi}_{3*}(\zeta) - \boldsymbol{M}_1\boldsymbol{\varphi}_1(\zeta) & |\zeta| > R_2^2/R_1 \end{cases} \tag{25}$$

Now we derive the solutions for the three cases that the dislocation is located in Materials 1, Material 2 and the inclusion, respectively.

### 3.2. Dislocation inside Material 1

Analyzing the singularities of complex potentials in three regions, it is seen that the complex potentials $\boldsymbol{f}_2(z)$ and $\boldsymbol{f}_3(z)$ are holomorphic in their domains and the complex potential $\boldsymbol{f}_1(z)$ can be written as

$$\boldsymbol{f}_1(z) = \boldsymbol{B}\ln(z - z_0) + \boldsymbol{f}_{10}(z) \quad z \in S_1 \tag{26}$$

where $\boldsymbol{B} = \boldsymbol{b}/(2\pi i)$ and $\boldsymbol{f}_{10}(z)$ is holomorphic in its domain. The substitution of Equations (9) and (12) into Equation (26) yields

$$\boldsymbol{\varphi}_1(\zeta) = \boldsymbol{B}\ln\frac{\zeta - \zeta_0}{\zeta + R_2} + \boldsymbol{\varphi}_{10}(\zeta) \quad |\zeta| > R_2 \tag{27}$$

From Equation (16), we have

$$\boldsymbol{\varphi}_{1*}(\zeta) = \frac{\boldsymbol{b}}{2\pi i}\ln\frac{\zeta - R_2^2/\bar{\zeta}_0}{\zeta + R_2} + \boldsymbol{\varphi}_{1*0}(\zeta) \quad |\zeta| < R_2 \tag{28}$$

Neglecting the constant terms representing the rigid displacement and equipotential field, the complex potential $\boldsymbol{\varphi}_2(\zeta)$ can be expanded into Laurent series in the annular region:

$$\boldsymbol{\varphi}_2(\zeta) = \boldsymbol{G}_P(\zeta) + \boldsymbol{G}_N(\zeta) = \sum_{n=1}^{\infty} \boldsymbol{a}_n\zeta^n + \sum_{n=1}^{\infty} \boldsymbol{b}_n\zeta^{-n} \quad R_1 < |\zeta| < R_2 \tag{29}$$

where $\boldsymbol{a}_n$ and $\boldsymbol{b}_n$ are the complex coefficient vectors to be determined. From Equations (17) and (18), two function vectors can be obtained:

$$\boldsymbol{\varphi}_{2*}(\zeta) = -\bar{\boldsymbol{G}}_P(R_2^2/\zeta) - \bar{\boldsymbol{G}}_N(R_2^2/\zeta) \quad R_2 < |\zeta| < R_2^2/R_1 \tag{30}$$

$$\boldsymbol{\varphi}_{2**}(\zeta) = -\bar{\boldsymbol{G}}_P(R_1^2/\zeta) - \bar{\boldsymbol{G}}_N(R_1^2/\zeta) \quad R_1^2/R_2 < |\zeta| < R_1 \tag{31}$$
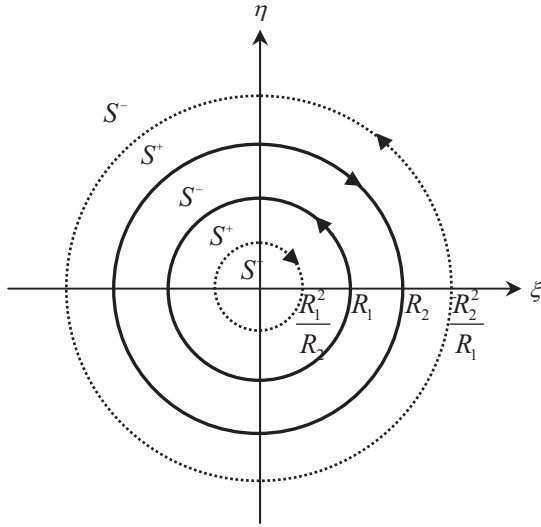
**Figure 2.** Domain of the sectionally holomorphic functions $\Psi_{U0}(\zeta)$ and $\Psi_{T0}(\zeta)$.

It is obvious that $\varphi_3(\zeta)$ and $\varphi_{3^*}(\zeta)$ also are holomorphic in their domains. Now we can obtain two sectional holomorphic function vectors from Equations (22)–(25):

$$\Psi_{U0}(\zeta) = \begin{cases} \varphi_{1^*0}(\zeta) + \varphi_3(\zeta) & |\zeta| < R_1^2/R_2 \\ \varphi_{1^*0}(\zeta) + \varphi_{2^{**}}(\zeta) + \varphi_3(\zeta) & R_1^2/R_2 < |\zeta| < R_1 \\ \varphi_{1^*0}(\zeta) + \varphi_2(\zeta) + \varphi_{3^*}(\zeta) & R_1 < |\zeta| < R_2 \\ \varphi_{10}(\zeta) + \varphi_{2^*}(\zeta) + \varphi_{3^*}(\zeta) & R_2 < |\zeta| < R_2^2/R_1 \\ \varphi_{10}(\zeta) + \varphi_{3^*}(\zeta) & |\zeta| > R_2^2/R_1 \end{cases} \tag{32}$$

$$\Psi_{T0}(\zeta) = \begin{cases} M_1\varphi_{1^*0}(\zeta) - M_3\varphi_3(\zeta) & |\zeta| < R_1^2/R_2 \\ M_1\varphi_{1^*0}(\zeta) + M_2\varphi_{2^{**}}(\zeta) - M_3\varphi_3(\zeta) & R_1^2/R_2 < |\zeta| < R_1 \\ M_1\varphi_{1^*0}(\zeta) - M_2\varphi_2(\zeta) + M_3\varphi_{3^*}(\zeta) & R_1 < |\zeta| < R_2 \\ M_2\varphi_{2^*}(\zeta) - M_1\varphi_{10}(\zeta) + M_3\varphi_{3^*}(\zeta) & R_2 < |\zeta| < R_2^2/R_1 \\ M_3\varphi_{3^*}(\zeta) - M_1\varphi_{10}(\zeta) & |\zeta| > R_2^2/R_1 \end{cases} \tag{33}$$

where defined domains are as shown in Figure 2 and boundary conditions can be written as

$$\Psi_{U0}^+(t) - \Psi_{U0}^-(t) = \begin{cases} -\bar{G}_P(R_1^2/t) - \bar{G}_N(R_1^2/t) & |t| = R_1^2/R_2 \\ 0 & |t| = R_1 \\ B\ln\frac{t - R_2^2/\bar{\zeta}_0}{t + R_1^2/R_2} - B\ln\frac{t - \zeta_0}{t + R_2} & |t| = R_2 \\ -\bar{G}_P(R_2^2/t) - \bar{G}_N(R_2^2/t) & |t| = R_2^2/R_1 \end{cases} \tag{34}$$

$$\Psi_{T0}^+(t) - \Psi_{T0}^-(t) = \begin{cases} -M_2\bar{G}_P(R_1^2/t) - M_2\bar{G}_N(R_1^2/t) & |t| = R_1^2/R_2 \\ 0 & |t| = R_1 \\ M_1 B\ln\frac{t - R_2^2/\bar{\zeta}_0}{t + R_1^2/R_2} + M_1 B\ln\frac{t - \zeta_0}{t + R_2} & |t| = R_2 \\ -M_2\bar{G}_P(R_2^2/t) - M_2\bar{G}_N(R_2^2/t) & |t| = R_2^2/R_1 \end{cases} \tag{35}$$

where $B = 1/(2\pi i)b = 1/(2\pi i)\{b_w, b_\phi\}^T$ and the superscripts " $+$ " and " $-$ " represent the function vector boundary values as approached from regions $S^+$ and $S^-$, respectively, as shown in Figure 2. Now the problem is reduced to the boundary value problem of two sectionally holomorphic function vectors $\Psi_{U0}(\zeta)$ and $\Psi_{T0}(\zeta)$.

According to the work of Muskhelishvili [35], the above problem can be solved by the Cauchy integrals. From Equations (34) and (35), we can obtain

$$
\begin{aligned}
\boldsymbol{\Psi}_{U0} &= \boldsymbol{\varphi}_{1^*0}(\zeta) + \boldsymbol{\varphi}_3(\zeta) \\
&= \bar{\boldsymbol{G}}_N(R_1^2/\zeta) + \boldsymbol{B}\ln\frac{\zeta - \zeta_0}{\zeta + R_2} - \bar{\boldsymbol{G}}_N(R_2^2/\zeta) \qquad |\zeta| < R_1^2/R_2
\end{aligned} \tag{36}
$$

$$
\begin{aligned}
\boldsymbol{\Psi}_{U0} &= \boldsymbol{\varphi}_{1^*0}(\zeta) + \boldsymbol{\varphi}_2(\zeta) + \boldsymbol{\varphi}_{3^*}(\zeta) \\
&= -\bar{\boldsymbol{G}}_P(R_1^2/\zeta) + \boldsymbol{B}\ln\frac{\zeta - \zeta_0}{\zeta + R_2} - \bar{\boldsymbol{G}}_N(R_2^2/\zeta) \qquad R_1 < |\zeta| < R_2
\end{aligned} \tag{37}
$$

$$
\begin{aligned}
\boldsymbol{\Psi}_{U0}(\zeta) &= \boldsymbol{\varphi}_{10}(\zeta) + \boldsymbol{\varphi}_{3^*}(\zeta) \\
&= -\bar{\boldsymbol{G}}_P(R_1^2/\zeta) + \boldsymbol{B}\ln\frac{\zeta - R_2^2/\bar{\zeta}_0}{\zeta + R_1^2/R_2} + \bar{\boldsymbol{G}}_P(R_2^2/\zeta) \qquad |\zeta| > R_2^2/R_1
\end{aligned} \tag{38}
$$

$$
\begin{aligned}
\boldsymbol{\Psi}_{T0} &= \boldsymbol{M}_1\boldsymbol{\varphi}_{1^*0}(\zeta) - \boldsymbol{M}_3\boldsymbol{\varphi}_3(\zeta) \\
&= \boldsymbol{M}_2\bar{\boldsymbol{G}}_N(R_1^2/\zeta) - \boldsymbol{M}_1\boldsymbol{B}\ln\frac{\zeta - \zeta_0}{\zeta + R_2} - \boldsymbol{M}_2\bar{\boldsymbol{G}}_N(R_2^2/\zeta) \qquad |\zeta| < R_1^2/R_2
\end{aligned} \tag{39}
$$

$$
\begin{aligned}
\boldsymbol{\Psi}_{T0} &= \boldsymbol{M}_1\boldsymbol{\varphi}_{1^*0}(\zeta) - \boldsymbol{M}_2\boldsymbol{\varphi}_2(\zeta) + \boldsymbol{M}_3\boldsymbol{\varphi}_{3^*}(\zeta) \\
&= -\boldsymbol{M}_2\bar{\boldsymbol{G}}_P(R_1^2/\zeta) - \boldsymbol{M}_1\boldsymbol{B}\ln\frac{\zeta - \zeta_0}{\zeta + R_2} - \boldsymbol{M}_2\bar{\boldsymbol{G}}_N(R_2^2/\zeta) \qquad R_1 < |\zeta| < R_2
\end{aligned} \tag{40}
$$

$$
\begin{aligned}
\boldsymbol{\Psi}_{T0} &= \boldsymbol{M}_3\boldsymbol{\varphi}_{3^*}(\zeta) - \boldsymbol{M}_1\boldsymbol{\varphi}_{10}(\zeta) \\
&= -\boldsymbol{M}_2\bar{\boldsymbol{G}}_P(R_1^2/\zeta) + \boldsymbol{M}_1\boldsymbol{B}\ln\frac{\zeta - R_2^2/\bar{\zeta}_0}{\zeta + R_2} + \boldsymbol{M}_2\bar{\boldsymbol{G}}_P(R_2^2/\zeta) \qquad |\zeta| > R_2^2/R_1
\end{aligned} \tag{41}
$$

From Equations (36) and (39), we have

$$
\begin{aligned}
\boldsymbol{\varphi}_3(\zeta) = {}& 2(\boldsymbol{M}_1 + \boldsymbol{M}_3)^{-1}\boldsymbol{M}_1\boldsymbol{B}\ln\frac{\zeta - \zeta_0}{\zeta + R_2} + (\boldsymbol{M}_1 + \boldsymbol{M}_3)^{-1}(\boldsymbol{M}_1 - \boldsymbol{M}_2)\bar{\boldsymbol{G}}_N(R_1^2/\zeta) \\
&+ (\boldsymbol{M}_1 + \boldsymbol{M}_3)^{-1}(\boldsymbol{M}_2 - \boldsymbol{M}_1)\bar{\boldsymbol{G}}_N(R_2^2/\zeta)
\end{aligned} \tag{42}
$$

From Equations (38) and (41), we have

$$
\begin{aligned}
\boldsymbol{\varphi}_1(\zeta) = {}& \boldsymbol{B}\ln\frac{\zeta - \zeta_0}{\zeta + R_2} + (\boldsymbol{M}_1 + \boldsymbol{M}_3)^{-1}(\boldsymbol{M}_3 - \boldsymbol{M}_1)\boldsymbol{B}ln\frac{\zeta - R_2^2/\bar{\zeta}_0}{\zeta + R_2} \\
&+ (\boldsymbol{M}_1 + \boldsymbol{M}_3)^{-1}(\boldsymbol{M}_2 - \boldsymbol{M}_3)\bar{\boldsymbol{G}}_P(R_1^2/\zeta) + (\boldsymbol{M}_1 + \boldsymbol{M}_3)^{-1}(\boldsymbol{M}_3 - \boldsymbol{M}_2)\bar{\boldsymbol{G}}_P(R_2^2/\zeta)
\end{aligned} \tag{43}
$$

It can be seen that the complex potentials $\boldsymbol{\varphi}_1(\zeta)$ and $\boldsymbol{\varphi}_3(\zeta)$ are related to the complex potential $\boldsymbol{\varphi}_2(\zeta) = \boldsymbol{G}_P(\zeta) + \boldsymbol{G}_N(\zeta)$. The remaining task is to determine the complex potential $\boldsymbol{\varphi}_2(\zeta)$. From Equations (36)–(41) the following equation can be derived:

$$
\begin{aligned}
&(\boldsymbol{M}_2 + \boldsymbol{M}_3)[\boldsymbol{G}_P(\zeta) + \boldsymbol{G}_N(\zeta)] + (\boldsymbol{M}_3 - \boldsymbol{M}_2)\bar{\boldsymbol{G}}_P(R_1^2/\zeta) + (\boldsymbol{M}_3 - \boldsymbol{M}_2)\bar{\boldsymbol{G}}_N(R_2^2/\zeta) \\
&+ (\boldsymbol{M}_3 - \boldsymbol{M}_1)(\boldsymbol{M}_1 + \boldsymbol{M}_3)^{-1}(\boldsymbol{M}_2 + \boldsymbol{M}_3)\bar{\boldsymbol{G}}_N(R_1^2/\zeta) + (\boldsymbol{M}_1 - \boldsymbol{M}_3)(\boldsymbol{M}_1 + \boldsymbol{M}_3)^{-1}(\boldsymbol{M}_2 + \boldsymbol{M}_3)\bar{\boldsymbol{G}}_N(R_2^2/\zeta) \\
&= \left[(\boldsymbol{M}_1 - \boldsymbol{M}_3)(\boldsymbol{M}_1 + \boldsymbol{M}_3)^{-1}(\boldsymbol{M}_3 - \boldsymbol{M}_1) + (\boldsymbol{M}_3 + \boldsymbol{M}_1)\right]\boldsymbol{B}\ln\frac{\zeta - \zeta_0}{\zeta + R_2} \qquad R_1 < |\zeta| < R_2
\end{aligned} \tag{44}
$$

Noting that

$$\ln\frac{\zeta-\zeta_0}{\zeta+R_2}=\ln\frac{1-\zeta/\zeta_0}{1+\zeta/R_2}=\sum_{n=1}^{\infty}\frac{(-1)^nR_2^{-n}-\zeta_0^{-n}}{n}\cdot\zeta^n \quad R_1<|\zeta|<R_2 \tag{45}$$

where the constant terms are neglected, which represent the rigid displacement and equipotential field. The substitution of Equation (45) into Equation (44) and the comparison of coefficients of the same power terms yield the explicit expressions of the coefficients:

$$\boldsymbol{a}_n=\boldsymbol{K}^{-1}\boldsymbol{JB}\frac{(-1)^nR_2^{-n}-\zeta_0^{-n}}{n} \tag{46}$$

$$\boldsymbol{b}_n=(\boldsymbol{M}_2+\boldsymbol{M}_3)^{-1}(\boldsymbol{M}_3-\boldsymbol{M}_2)\boldsymbol{K}^{-1}\boldsymbol{JB}\frac{(-1)^nR_1^{2n}R_2^{-n}-\bar{\zeta}_0^{-n}R_1^{2n}}{n} \tag{47}$$

where

$$\begin{aligned}\boldsymbol{K}=&(\boldsymbol{M}_3-\boldsymbol{M}_1)(\boldsymbol{M}_1+\boldsymbol{M}_3)^{-1}(\boldsymbol{M}_2-\boldsymbol{M}_3)+\boldsymbol{M}_2+\boldsymbol{M}_3\\&+(\boldsymbol{M}_3-\boldsymbol{M}_2)(\boldsymbol{M}_2+\boldsymbol{M}_3)^{-1}(\boldsymbol{M}_2-\boldsymbol{M}_3)R_1^{2n}R_2^{-2n}\\&+(\boldsymbol{M}_1-\boldsymbol{M}_3)(\boldsymbol{M}_1+\boldsymbol{M}_3)^{-1}(\boldsymbol{M}_2-\boldsymbol{M}_3)R_1^{2n}R_2^{-2n}\end{aligned} \tag{48}$$

$$\boldsymbol{J}=(\boldsymbol{M}_1-\boldsymbol{M}_3)(\boldsymbol{M}_1+\boldsymbol{M}_3)^{-1}(\boldsymbol{M}_3-\boldsymbol{M}_1)+(\boldsymbol{M}_1+\boldsymbol{M}_3) \tag{49}$$

The electroelastic field variables in Material 1, Material 2 and the inclusion can be evaluated by means of Equations (4) and (5).

### 3.3. Dislocation inside Material 2

Using the similar method in the above section, when a piezoelectric screw dislocation is located at $z=z_0$ inside Material 2, the complex potentials can be derived as

$$\begin{aligned}\boldsymbol{\varphi}_1(\zeta)=&(\boldsymbol{M}_1+\boldsymbol{M}_3)^{-1}(\boldsymbol{M}_2+\boldsymbol{M}_3)\boldsymbol{B}\frac{\zeta-\zeta_0}{\zeta+R_2}+(\boldsymbol{M}_1+\boldsymbol{M}_3)^{-1}(\boldsymbol{M}_3-\boldsymbol{M}_2)\boldsymbol{B}\ln\frac{\zeta-R_1^2/\bar{\zeta}_0}{\zeta+R_1^2/R_2}\\&+(\boldsymbol{M}_1+\boldsymbol{M}_3)^{-1}(\boldsymbol{M}_2-\boldsymbol{M}_3)\bar{\boldsymbol{G}}'_P(R_1^2/\zeta)+(\boldsymbol{M}_1+\boldsymbol{M}_3)^{-1}(\boldsymbol{M}_3-\boldsymbol{M}_2)\bar{\boldsymbol{G}}'_P(R_2^2/\zeta)\end{aligned} \tag{50}$$

$$\begin{aligned}\boldsymbol{\varphi}_3(\zeta)=&(\boldsymbol{M}_1+\boldsymbol{M}_3)^{-1}(\boldsymbol{M}_1+\boldsymbol{M}_2)\boldsymbol{B}\ln\frac{\zeta-\zeta_0}{\zeta+R_2}+(\boldsymbol{M}_1+\boldsymbol{M}_3)^{-1}(\boldsymbol{M}_1-\boldsymbol{M}_2)\boldsymbol{B}\ln\frac{\zeta-R_2^2/\bar{\zeta}_0}{\zeta+R_2}\\&+(\boldsymbol{M}_1+\boldsymbol{M}_3)^{-1}(\boldsymbol{M}_1-\boldsymbol{M}_2)\bar{\boldsymbol{G}}'_N(R_1^2/\zeta)+(\boldsymbol{M}_1+\boldsymbol{M}_3)^{-1}(\boldsymbol{M}_2-\boldsymbol{M}_1)\bar{\boldsymbol{G}}'_N(R_2^2/\zeta)\end{aligned} \tag{51}$$

$$\boldsymbol{\varphi}_2(\zeta)=\boldsymbol{B}\ln\frac{\zeta-\zeta_0}{\zeta+R_2}+\boldsymbol{G}'_P(\zeta)+\boldsymbol{G}'_N(\zeta) \tag{52}$$

where

$$\boldsymbol{G}'_P(\zeta)=\sum_{n=1}^{\infty}\boldsymbol{a}'_n\zeta^n \text{ and } \boldsymbol{G}'_N(\zeta)=\sum_{n=1}^{\infty}\boldsymbol{b}'_n\zeta^{-n} \tag{53}$$

The explicit expressions of the coefficients $\boldsymbol{a}'_n$ and $\boldsymbol{b}'_n$ are

$$\boldsymbol{a}'_n=(\boldsymbol{M}_1+\boldsymbol{M}_2)^{-1}(\boldsymbol{M}_1-\boldsymbol{M}_2)\boldsymbol{B}\frac{(-1)^nR_2^{-n}-\bar{\zeta}_0^nR_2^{-2n}}{n}+(\boldsymbol{M}_1+\boldsymbol{M}_2)^{-1}(\boldsymbol{M}_2-\boldsymbol{M}_1)\bar{\boldsymbol{b}}'_nR_2^{-2n} \tag{54}$$

$$\boldsymbol{b}'_n=(\boldsymbol{K}')^{-1}\boldsymbol{LB}\frac{(-1)^nR_2^n-R_2^{2n}\bar{\zeta}_0^{-n}}{n}+(\boldsymbol{K}')^{-1}\boldsymbol{J}'\boldsymbol{B}\frac{(-1)^nR_2^n-\zeta_0^n}{n} \tag{55}$$

where

$$K' = [(M_1 - M_3)(M_1 + M_3)^{-1}(M_2 - M_1) + (M_1 + M_2)]R_1^{-2n}R_2^{2n}$$
$$+ (M_1 - M_2)(M_1 + M_2)^{-1}(M_2 - M_1) + (M_3 - M_1)(M_1 + M_3)^{-1}(M_2 - M_1) \tag{56}$$

$$J' = (M_1 - M_3)(M_1 + M_3)^{-1}(M_2 - M_1) + (M_2 - M_1)(M_1 + M_2)^{-1}(M_2 - M_1) \tag{57}$$

$$L = (M_3 - M_1)(M_1 + M_3)^{-1}(M_1 + M_2) + (M_1 - M_2) \tag{58}$$

### 3.4. Dislocation inside Inclusion

Similarly, when a screw dislocation is located at $z = z_0$ inside the inclusion, the complex potentials can be derived as

$$\varphi_1(\zeta) = (M_1 + M_3)^{-1}(M_2 + M_3)B\ln\frac{\zeta - \zeta_0}{\zeta + R_2} + (M_1 + M_3)^{-1}(M_3 - M_2)B\ln\frac{\zeta - \zeta_0}{\zeta + R_1^2/R_2}$$
$$+ (M_1 + M_3)^{-1}(M_2 - M_3)\bar{G}''_P(R_1^2/\zeta) + (M_1 + M_3)^{-1}(M_3 - M_2)\bar{G}''_P(R_2^2/\zeta) \tag{59}$$

$$\varphi_3(\zeta) = B\ln\frac{\zeta - \zeta_0}{\zeta + R_2} + (M_1 + M_3)^{-1}(M_2 - M_3)B\ln\frac{\zeta - R_1^2/\bar{\zeta}_0}{\zeta + R_2}$$
$$+ (M_1 + M_3)^{-1}(M_1 - M_2)B\ln\frac{\zeta - R_2^2/\bar{\zeta}_0}{\zeta + R_2} + (M_1 + M_3)^{-1}(M_1 - M_2)\bar{G}''_N(R_1^2/\zeta)$$
$$+ (M_1 + M_3)^{-1}(M_2 - M_1)\bar{G}''_N(R_2^2/\zeta) \tag{60}$$

$$\varphi_2(\zeta) = B\ln\frac{\zeta - \zeta_0}{\zeta + R_2} + G''_P(\zeta) + G''_N(\zeta) \tag{61}$$

where

$$G''_P(\zeta) = \sum_{n=1}^{\infty} a''_n\zeta^n \text{ and } G''_N(\zeta) = \sum_{n=1}^{\infty} b''_n\zeta^{-n} \tag{62}$$

The explicit expressions of the coefficients $a''$ and $b''_n$ are

$$a''_n = (M_1 + M_2)^{-1}(M_1 - M_2)B\frac{(-1)^n R_2^{-n} - \bar{\zeta}_0^n R_2^{-2n}}{n} + (M_1 + M_2)^{-1}(M_2 - M_1)\bar{b}''_n R_2^{-2n} \tag{63}$$

$$b''_n = (K'')^{-1}J''B\frac{(-1)^n R_1^{2n}R_2^{-n} - R_1^{2n}R_2^{-2n}\zeta_0^n}{n} + (K'')^{-1}L'B\frac{(-1)^n R_2^{-n}R_1^{2n} - \zeta_0^n}{n} \tag{64}$$

where

$$K'' = (M_1 - M_3)(M_1 + M_3)^{-1}(M_2 - M_1) + M_1 + M_2$$
$$+ (M_3 - M_1)(M_1 + M_3)^{-1}(M_2 - M_1)R_1^{2n}R_2^{-2n}$$
$$+ (M_1 - M_2)(M_1 + M_2)^{-1}(M_2 - M_1)R_1^{2n}R_2^{-2n} \tag{65}$$

$$J'' = (M_1 - M_3)(M_1 + M_3)^{-1}(M_2 - M_1)$$
$$+ (M_2 - M_1)(M_1 + M_2)^{-1}(M_2 - M_1) \tag{66}$$

$$L' = (M_3 - M_1)(M_1 + M_3)^{-1}(M_2 - M_3) + M_3 - M_2 \tag{67}$$

## 4. Special cases and separation of coupling interaction effects

In this section we will examine some special cases of the present solutions, which is not only to check the correctness of the solutions, but also to seek new expressions of physical significance (various interaction effects are separated) and of mathematical elegance (much better convergence).

Consider the typical case that the dislocation is located in Material 1. By using the inverse transformation (11) and neglecting constant terms, we can obtain the following transformation formulae between the two planes:

$$\ln \frac{\zeta - \zeta_0}{\zeta + R_2} \to \ln (z - z_0), \ \ \ln \frac{\zeta - R_1^2/\bar{\zeta}_0}{\zeta + R_1^2/R_2} \to \ln \left(\frac{R_1^2}{z} - \bar{z}_0\right), \ \ \ln \frac{\zeta - R_2^2/\bar{\zeta}_0}{\zeta + R_2} \to \ln[z + \bar{z}_0 - 2(R_1 + h)] \tag{68}$$

When $M_1 = M_2 = M_3$, the solutions (29), (42) and (43) degenerate into

$$\boldsymbol{\varphi}_1(\zeta) = \boldsymbol{\varphi}_2(\zeta) = \boldsymbol{\varphi}_3(\zeta) = \boldsymbol{B} \ln \frac{\zeta - \zeta_0}{\zeta + R_2} \tag{69}$$

Noting the first formula of Equation (68), it is seen that Equation (69) is the solution for a piezoelectric screw dislocation in an infinite matrix, which is in agreement with the result in [21]. When $M_1 = M_2$, the solutions (29), (42) and (43) degenerate into

$$\boldsymbol{\varphi}_1(\zeta) = \boldsymbol{\varphi}_2(\zeta) = \boldsymbol{B} \ln \frac{\zeta - \zeta_0}{\zeta + R_2} + (M_2 + M_3)^{-1}(M_3 - M_2)\boldsymbol{B} \ln \frac{\zeta - R_1^2/\bar{\zeta}_0}{\zeta + R_1^2/R_2} \tag{70}$$

$$\boldsymbol{\varphi}_3(\zeta) = 2(M_2 + M_3)^{-1}M_2\boldsymbol{B} \ln \frac{\zeta - \zeta_0}{\zeta + R_2} \tag{71}$$

which are the solutions for a piezoelectric screw dislocation in an infinite matrix interacting with a circular inclusion. Noting the first and second formulae of Equation (68), they are identical to the results in [23,25]. When $M_3 = M_2$, the solutions (29), (42) and (43) degenerate into

$$\boldsymbol{\varphi}_1(\zeta) = \boldsymbol{B} \ln \frac{\zeta - \zeta_0}{\zeta + R_2} + (M_1 + M_2)^{-1}(M_2 - M_1)\boldsymbol{B} \ln \frac{\zeta - R_2^2/\bar{\zeta}_0}{\zeta + R_2} \tag{72}$$

$$\boldsymbol{\varphi}_2(\zeta) = \boldsymbol{\varphi}_3(\zeta) = 2(M_1 + M_2)^{-1}M_1\boldsymbol{B} \ln \frac{\zeta - \zeta_0}{\zeta + R_2} \tag{73}$$

which are the solutions of a piezoelectric screw dislocation interacting with the bimaterial interface. Noting the first and third formulae of Equation (68), they are in agreement with the results in [22].

Equation (70) shows that $\boldsymbol{\varphi}_1(\zeta)$ is made up of two terms, that is, the basic singular solution of a piezoelectric screw dislocation in an infinite matrix (Equation (69)) and an interaction term of the dislocation with a circular inclusion. Equation (72) shows that $\boldsymbol{\varphi}_1(\zeta)$ is made up of the basic singular solution and an interaction term of the dislocation with the bimaterial interface. The facts give us a significant hint that the complex potential $\boldsymbol{\varphi}_1(\zeta)$ in Equation (43) can be cast into a new expression:

$$\begin{aligned} \boldsymbol{\varphi}_{1\text{New}}(\zeta) = &\boldsymbol{B} \ln \frac{\zeta - \zeta_0}{\zeta + R_2} + (M_2 + M_3)^{-1}(M_3 - M_2)\boldsymbol{B} \ln \frac{\zeta - R_1^2/\bar{\zeta}_0}{\zeta + R_1^2/R_2} \\ &+ (M_1 + M_2)^{-1}(M_2 - M_1)\boldsymbol{B} \ln \frac{\zeta - R_2^2/\bar{\zeta}_0}{\zeta + R_2} + \boldsymbol{\varphi}_{\text{Cpl}}(\zeta) \end{aligned} \quad \zeta_0 \in S_1' \tag{74}$$

A comparison of Equation (74) with Equation (43) yields the explicit expression of $\boldsymbol{\varphi}_{1\text{Cpl}}(\zeta)$:

$$\boldsymbol{\varphi}_{1\text{Cpl}}(\zeta) = \sum_{n=1}^{\infty} [(\boldsymbol{M}_1 + \boldsymbol{M}_3)^{-1}(\boldsymbol{M}_2 - \boldsymbol{M}_3)\boldsymbol{K}^{-1}\boldsymbol{J}(R_2^{2n} - R_1^{2n}) + (\boldsymbol{M}_2 + \boldsymbol{M}_3)^{-1}(\boldsymbol{M}_2 - \boldsymbol{M}_3)R_1^{2n}$$
$$+ (\boldsymbol{M}_1 + \boldsymbol{M}_2)^{-1}(\boldsymbol{M}_1 - \boldsymbol{M}_2)R_2^{2n} + (\boldsymbol{M}_1 + \boldsymbol{M}_3)^{-1}(\boldsymbol{M}_3 - \boldsymbol{M}_1)R_2^{2n}]$$
$$\times \boldsymbol{B}\frac{((-1)^n R_2^{-n} - \bar{\zeta}_0^{-n})}{n}\zeta^{-n} \tag{75}$$

Apparently, $\boldsymbol{\varphi}_{1\text{Cpl}}(\zeta)$ represents a coupling interaction effect of the screw dislocation with the circular inclusion and bimaterial interface and it goes into zero when $\boldsymbol{M}_1 = \boldsymbol{M}_2$ or $\boldsymbol{M}_2 = \boldsymbol{M}_3$. $\boldsymbol{\varphi}_{1\text{Cpl}}(\zeta)$ is also the only infinite series in Equation (74).

Similarly, for the case that the dislocation is located in Material 2, we obtain

$$\boldsymbol{\varphi}_{2\text{New}}(\zeta) = \boldsymbol{B}\ln(\zeta - \zeta_0)/(\zeta + R_2) + (\boldsymbol{M}_2 + \boldsymbol{M}_3)^{-1}(\boldsymbol{M}_3 - \boldsymbol{M}_2)\boldsymbol{B}\ln\frac{\zeta - R_1^2/\bar{\zeta}_0}{\zeta + R_1^2/R_2}$$
$$+ (\boldsymbol{M}_1 + \boldsymbol{M}_2)^{-1}(\boldsymbol{M}_1 - \boldsymbol{M}_2)\boldsymbol{B}\ln\frac{\zeta - R_2^2/\bar{\zeta}_0}{\zeta + R_2} + \boldsymbol{\varphi}_{2\text{Cpl}}(\zeta) \qquad \zeta_0 \in S_2' \tag{76}$$

where

$$\boldsymbol{\varphi}_{2\text{Cpl}}(\zeta) = \sum_{n=1}^{\infty} \left\{ (\boldsymbol{K}')^{-1}\boldsymbol{J}'\boldsymbol{B}\frac{(-1)^n R_2^n - \zeta_0^n}{n} + [(\boldsymbol{K}')^{-1}\boldsymbol{L}R_2^{2n} + (\boldsymbol{M}_2 + \boldsymbol{M}_3)^{-1}(\boldsymbol{M}_2 - \boldsymbol{M}_3)R_1^{2n}] \right.$$
$$\left. \times \boldsymbol{B}\frac{(-1)^n R_2^{-n} - \bar{\zeta}_0^{-n}}{n} \right\}\zeta^{-n}$$
$$+ \sum_{n=1}^{\infty} \left\{ (\boldsymbol{M}_1 + \boldsymbol{M}_2)^{-1}(\boldsymbol{M}_1 - \boldsymbol{M}_2)(\boldsymbol{K}')^{-1}\boldsymbol{J}'\boldsymbol{B}\frac{(-1)^n R_2^{-n} - R_2^{-2n}\bar{\zeta}_0^n}{n} \right.$$
$$+ (\boldsymbol{M}_1 + \boldsymbol{M}_2)^{-1}(\boldsymbol{M}_1 - \boldsymbol{M}_2)(\boldsymbol{K}')^{-1}\boldsymbol{L} \times \boldsymbol{B}\frac{(-1)^n R_2^{-n} - \zeta_0^{-n}}{n} \right\}\zeta^n \tag{77}$$

For the case that the dislocation is located in the inclusion, we have

$$\boldsymbol{\varphi}_{3\text{New}}(\zeta) = \boldsymbol{B}\ln\frac{\zeta - \zeta_0}{\zeta + R_2} + (\boldsymbol{M}_2 + \boldsymbol{M}_3)^{-1}(\boldsymbol{M}_2 - \boldsymbol{M}_3)\boldsymbol{B}\ln\frac{\zeta - R_1^2/\bar{\zeta}_0}{\zeta + R_2}$$
$$+ (\boldsymbol{M}_1 + \boldsymbol{M}_2)^{-1}(\boldsymbol{M}_1 - \boldsymbol{M}_2)\boldsymbol{B}\ln\frac{\zeta - R_2^2/\bar{\zeta}_0}{\zeta + R_2} + \boldsymbol{\varphi}_{3\text{Cpl}}(\zeta) \qquad \zeta_0 \in S_3' \tag{78}$$

where

$$\boldsymbol{\varphi}_{3\text{Cpl}}(\zeta) = \sum_{n=1}^{\infty} \left\{ (\boldsymbol{M}_1 + \boldsymbol{M}_3)^{-1}(\boldsymbol{M}_2 - \boldsymbol{M}_1)(\boldsymbol{K}'')^{-1}\boldsymbol{J}''(1 - R_1^{2n}R_2^{-2n}) \right.$$
$$\left. + [(\boldsymbol{M}_1 + \boldsymbol{M}_3)^{-1} - (\boldsymbol{M}_1 + \boldsymbol{M}_2)^{-1}](\boldsymbol{M}_1 - \boldsymbol{M}_2) \right\}\boldsymbol{B}\frac{(-1)^n R_2^{-n} - R_2^{-2n}\bar{\zeta}_0^n}{n}\zeta^n$$
$$+ \sum_{n=1}^{\infty} \left\{ (\boldsymbol{M}_1 + \boldsymbol{M}_3)^{-1}(\boldsymbol{M}_2 - \boldsymbol{M}_1)(\boldsymbol{K}'')^{-1}\boldsymbol{L}'(1 - R_1^{2n}R_2^{-2n}) \right.$$
$$\left. + [(\boldsymbol{M}_1 + \boldsymbol{M}_3)^{-1} - (\boldsymbol{M}_2 + \boldsymbol{M}_3)^{-1}](\boldsymbol{M}_3 - \boldsymbol{M}_2) \right\}\boldsymbol{B}\frac{(-1)^n R_2^{-n} - R_1^{-2n}\bar{\zeta}_0^n}{n}\zeta^n \tag{79}$$

From their physical meaning, Equations (75), (77), (79) representing coupling interaction effects are higher order interaction. Hence the new expressions (74), (76) and (78) of the solutions with separating

coupling interactions converge much more rapidly than the original expressions (43), (52) and (60), which will be further discussed in Section 5.2.

# 5. Image force

## 5.1. The generalized Peach–Koehler formula

The image force acting on dislocations is an important physical parameter in understanding electroelastic behavior of inhomogeneous material, especially in understanding the mobility and so-called trapping mechanism of the dislocation. According to the generalized Peach–Koehler formula [21], the image force can be evaluated by

$$F = F_x - \mathrm{i}F_y = \mathrm{i}\boldsymbol{b}^{\mathrm{T}}[\boldsymbol{\Sigma}_x^0 - \mathrm{i}\boldsymbol{\Sigma}_y^0] \tag{80}$$

where $F_x$ and $F_y$ are the image force components in the $x$-axis and $y$-axis directions, respectively; $\boldsymbol{\Sigma}_x^0$ and $\boldsymbol{\Sigma}_y^0$ denote the perturbation stress and electric displacement components at the dislocation point $z_0$. Noting Equations (14) and (80), we have

$$F_i = \mathrm{i}\boldsymbol{b}^{\mathrm{T}}\boldsymbol{M}_i[\boldsymbol{f}'_{i0}(z)]_{z=z_0} = \mathrm{i}\boldsymbol{b}^{\mathrm{T}}\boldsymbol{M}_i[\boldsymbol{\varphi}'_{i0}(\zeta)/m'(\zeta)]_{\zeta=\zeta_0} \quad \zeta_0 \in S'_i \tag{81}$$

where the index "$i$" takes values 1, 2 and 3 to refer to the three regions occupied by Material 1, Material 2 and the inclusion, respectively, and $\boldsymbol{\varphi}_{i0}(\zeta)$ is the holomorphic part of the complex potential in the region where the dislocation is located. It is noted that the image force, $F_i$, is a function of position coordinates of the dislocation.

## 5.2. Accuracy of solutions

In this section, numerical examples for image forces are presented to examine the accuracy of solutions. Set the size of the dislocation

$$\boldsymbol{b} = \left\{ b_w b_\phi \right\}^{\mathrm{T}} = \left\{ 1.0 \times 10^{-9}\mathrm{m} \quad 1.0\,\mathrm{V} \right\}^{\mathrm{T}} \tag{82}$$

We take the nondimensional distance $h/R_1 = 0.5$ and assume that Material 2 is the PZT-5H piezoelectric ceramic with electroelastic properties:

$$c_{44}^{(0)} = 3.53 \times 10^{10}\mathrm{N/m}^2, \; e_{15}^{(0)} = 17\mathrm{C/m}^2, \; \varepsilon_{11}^{(0)} = 1.51 \times 10^{-8}\mathrm{F/m} \tag{83}$$

Further we take $\boldsymbol{M}_1 = \lambda\boldsymbol{M}_2$ and $\boldsymbol{M}_3 = \upsilon\boldsymbol{M}_2$ to examine the general cases of mismatches in the material properties, where $\lambda$ and $\upsilon$ are two variable coefficients.

The image forces in the three regions are nondimensionalized by

$$F_{i0} = \frac{2\pi R_1}{c_{44}^{(0)} b_w^2} F_i \quad \zeta_0 \in S'_i \text{ or } z_0 \in S_i \tag{84}$$

where the index "$i$" takes values 1, 2 and 3 to refer to the three regions occupied by Material 1, Material 2 and the inclusion, respectively, and $F_i$ refers to equation (81).

The convergence of solutions is of practical importance. Now we compare numerically the convergence of the nondimensional image force by using the original expressions $\varphi_i$ in Equations (43), (52) and (60) and the new expressions $\varphi_{i\mathrm{New}}$ in Equations (74), (76) and (78). The number of terms in series required at a 1% truncation error of the nondimensional image force $F_{i0}$ are list in Table 1 for different values of $\lambda$ and $\upsilon$ in the inclusion ($x/R_1 = -0.99$, 0 and 0.99, Figure 1(a)), Material 2 ($x/R_1 = -1.2$, $-1.01$, 1.01, 1.25 and 1.49) and Material 1 ($x/R_1 = 1.51$ and 1.7).

It can be seen from Table 1 that the convergence of the new expressions is much better than that of the original expressions, especially when the dislocation point is close to the interface $\Gamma_1$ or $\Gamma_2$. In most cases, one-order approximations of the new expressions can provide satisfactory accuracy.

**Table 1.** The number of terms in series required at a 1% truncation error of the nondimensional image force (refer to Equation (84)) for different values of $\lambda$ and $\upsilon$ in the inclusion ($x/R_1 = -0.99$, 0 and 0.99), Material 2 ($x/R_1 = -1.2$, $-1.01$, 1.01, 1.25 and 1.49) and Material 1 ($x/R_1 = 1.51$ and 1.7), where the nondimensional distance $h/R_1 = 0.5$ (refer to Figure 1(a)).

| | Number of terms | | | | | | | | | |
| | $x/R_1 = -1.2$ | | $x/R_1 = -1.01$ | | $x/R_1 = -0.99$ | | $x/R_1 = 0$ | | $x/R_1 = 0.99$ | |
| $M_1 = \lambda M_2$, $M_3 = \upsilon M_2$ | $\varphi_{2New}$ | $\varphi_2$ | $\varphi_{2New}$ | $\varphi_2$ | $\varphi_{3New}$ | $\varphi_3$ | $\varphi_{3New}$ | $\varphi_3$ | $\varphi_{3New}$ | $\varphi_3$ |
|---|---|---|---|---|---|---|---|---|---|---|
| $\lambda = 10$, $\upsilon = 10$ | 3 | 29 | 0 | 519 | 0 | 513 | 4 | 30 | 0 | 104 |
| $\lambda = 10$, $\upsilon = 0.1$ | 3 | 31 | 0 | 520 | 0 | 514 | 4 | 30 | 0 | 102 |
| $\lambda = 0.1$, $\upsilon = 10$ | 3 | 30 | 0 | 519 | 0 | 513 | 4 | 30 | 0 | 103 |
| $\lambda = 0.1$, $\upsilon = 0.1$ | 2 | 28 | 0 | 518 | 0 | 512 | 3 | 30 | 0 | 103 |

| | Number of terms | | | | | | | | | |
| | $x/R_1 = 1.01$ | | $x/R_1 = 1.25$ | | $x/R_1 = 1.49$ | | $x/R_1 = 1.51$ | | $x/R_1 = 1.7$ | |
| $M_1 = \lambda M_2$, $M_3 = \upsilon M_2$ | $\varphi_{2New}$ | $\varphi_2$ | $\varphi_{2New}$ | $\varphi_2$ | $\varphi_{2New}$ | $\varphi_2$ | $\varphi_{1New}$ | $\varphi_1$ | $\varphi_{1New}$ | $\varphi_1$ |
|---|---|---|---|---|---|---|---|---|---|---|
| $\lambda = 10$, $\upsilon = 10$ | 0 | 104 | 3 | 12 | 0 | 133 | 0 | 133 | 1 | 10 |
| $\lambda = 10$, $\upsilon = 0.1$ | 0 | 103 | 2 | 7 | 0 | 133 | 0 | 133 | 1 | 10 |
| $\lambda = 0.1$, $\upsilon = 10$ | 0 | 104 | 2 | 7 | 0 | 133 | 0 | 65 | 1 | 10 |
| $\lambda = 0.1$, $\upsilon = 0.1$ | 0 | 104 | 3 | 10 | 0 | 133 | 0 | 64 | 1 | 10 |
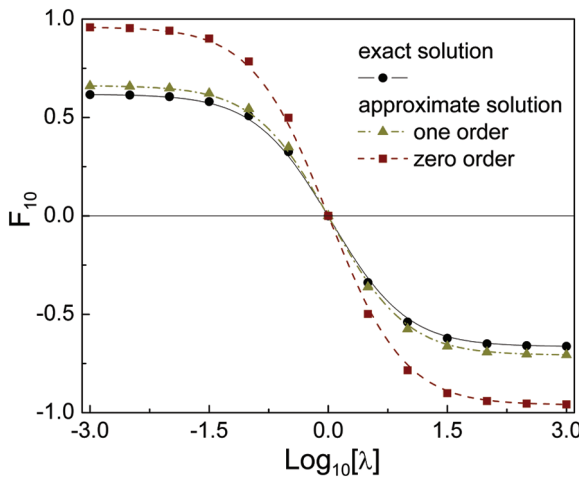


**Figure 3.** Nondimensional image force $F_{10}$ for the center of inclusion versus $\lambda$ by using the exact formula, first-order approximation and zero-order approximation, where $M_1 = \lambda M_2$, $M_3 = 2 M_2$ and $h/R_1 = 0.5$.

Let the dislocation locate at the center of the inclusion and take the parameter $\upsilon = 2$. The nondimensional image force $F_{30}$ (refer to Equation (84)) versus $\lambda$ is plotted in Figure 3 by using the exact formula (series number $n = 200$ in Equation (78)), first-order approximation ($n = 1$) and zero-order approximation ($n = 0$). It is observed that the maximum error of the zero-order approximation neglecting the coupling interaction is 55% in the whole value scope of $\lambda$, which shows that the coupling interaction cannot be ignored. When we use the first-order approximation accounting for the coupling interaction, the maximum error is reduced to 6%.

Further calculations show that the first-order approximation formulae of the new expressions have satisfactory accuracy in many cases. When the distance between the inclusion and the bimaterial interface is larger than the diameter of the inclusion, the coupling interaction is negligible, whereas when the distance is very small, more series terms are needed.
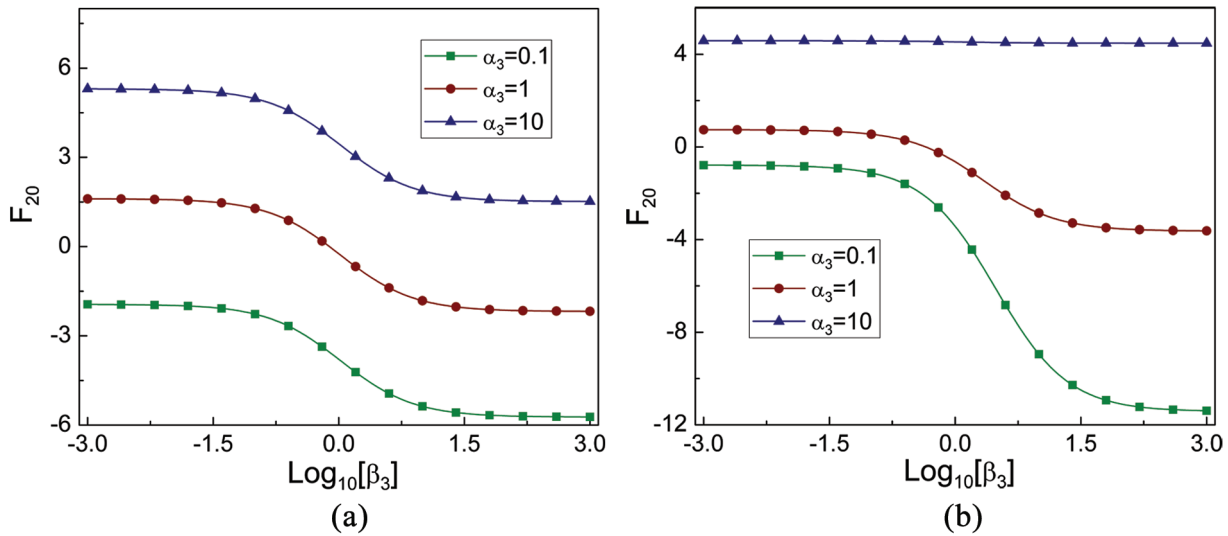
**Figure 4.** Nondimensional image force $F_{20}$ of the point $z_0/R_1 = 1.1$ versus $\beta_3$ for various values of $\alpha_3$, where $M_1 = 2M_2$, $c_{44}^{(3)} = \alpha_3 c_{44}^{(2)} = \alpha_3 c_{44}^{(0)} \varepsilon_{11}^{(3)} = \beta_3 \varepsilon_{11}^{(2)} = \beta_3 \varepsilon_{11}^{(0)}$ and $h/R_1 = 0.5$: (a) $e_{15}^{(3)} = e_{15}^{(2)} = 0$; (b) $e_{15}^{(3)} = e_{15}^{(2)} = e_{15}^{(0)}$.

# 6. Coupling interaction

The present solutions can help us to understand interesting and intricate coupling interaction phenomena, which arise from multiple material properties (mechanical, piezoelectric and dielectric properties) as well as from the geometry of multiple inhomogeneous phases.

For the convenience and concision of the discussion, we define three parameters, $\alpha_i$, $\beta_i$ and $\kappa_i$, to represent the mismatches of electro-elastic properties between the dissimilar materials in both sides of the inclusion/Material 2 interface and the bi-material interface:

$$\alpha_i = c_{44}^{(i)}/c_{44}^{(2)}, \quad \beta_i = \varepsilon_{11}^{(i)}/\varepsilon_{11}^{(2)}, \quad \kappa_i = e_{15}^{(i)}/e_{15}^{(2)} \tag{85}$$

where the index "$i$" takes values 1 and 3, and the superscripts (1), (2) and (3) refer to the electro-elastic properties in Material 1, Material 2 and the inclusion, respectively.

## 6.1. Coupling interaction arising from multiple material properties

Let the dislocation locate at the point $z_0/R_1 = 1.1$ in Material 2 and $h/R_1 = 0.5$ (refer to Figure 1(a)). In this section we take $M_1 = 2M_2$.

Firstly we consider the case that piezoelectric moduli of the inclusion and its surrounding material (Material 2) are the same. When the piezoelectric moduli of the two materials are zero, we have $e_{15}^{(1)} = e_{15}^{(2)} = e_{15}^{(3)} = 0$, $c_{44}^{(3)} = \alpha_3 c_{44}^{(2)}$ and $\varepsilon_{11}^{(3)} = \beta_3 \varepsilon_{11}^{(2)}$, where $\alpha_3$ and $\beta_3$ represent the mismatches of shear and dielectric moduli between the inclusion and Material 2 (refer to Equation (85)). The electro-elastic properties of Material 2 are $c_{44}^{(2)} = c_{44}^{(0)}$ and $\varepsilon_{11}^{(2)} = \varepsilon_{11}^{(0)}$ ($c_{44}^{(0)}$ and $\varepsilon_{11}^{(0)}$, refer to Equation (83)). The nondimensional image force $F_{20} = 2\pi R_1/(c_{44}^{(0)} b_w^2) F_2$ versus $\beta_3$ for various values of $\alpha_3$ is depicted in Figure 4(a). It is observed that the image force varies monotonically with the dielectric moduli, and the curves only have a translation for different shear moduli, which shows that the shear and dielectric moduli do not yield coupling effect when $e_{15}^{(1)} = e_{15}^{(2)} = e_{15}^{(3)} = 0$. The fact can be explained by Equations (76) and (81), from which the image force is a linear superposition of two fractional linear functions when the piezoelectric moduli of the three materials are zero.

When the piezoelectric moduli of the inclusion and Material 2 are not zero, we take that $e_{15}^{(3)} = e_{15}^{(2)} = e_{15}^{(0)}$. The nondimensional image force $F_{20}$ versus $\beta_3$ is depicted in Figure 4(b) for various values of $\alpha_3$. It is found that when the piezoelectric moduli are not zero, the shear and dielectric moduli yield a coupling effect.
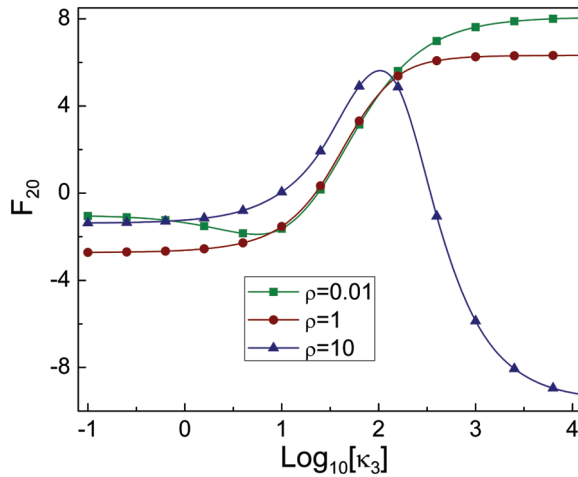
**Figure 5.** Nondimensional image force $F_{20}$ of the point $z_0/R_1 = 1.1$ versus $\kappa_3$ for various values of $\rho$, where $M_1 = 2M_2$, $c_{44}^{(3)} = c_{44}^{(2)} = c_{44}^{(0)}$, $e_{15}^{(3)} = \kappa_3 e_{15}^{(2)} = \kappa_3 e_{15}^{(0)}$, $\varepsilon_{11}^{(3)} = \varepsilon_{11}^{(2)} = \rho\varepsilon_{11}^{(0)}$ and $h/R_1 = 0.5$.

It is of interest to further examine the influence of the piezoelectric modulus on the image force. We assume that there are no mismatches of the shear and dielectric moduli between the inclusion and Material 2, but their piezoelectric moduli are different. Keep their shear moduli unchanged, that is, $c_{44}^{(3)} = c_{44}^{(2)} = c_{44}^{(0)}$, consider the variation of the dielectric moduli by a proportional coefficient $\rho$, that is, $\varepsilon_{11}^{(3)} = \varepsilon_{11}^{(2)} = \rho\varepsilon_{11}^{(0)}$, and introduce another ratio constant $\kappa_3 = e_{15}^{(3)}/e_{15}^{(2)}$ to present mismatches of piezoelectric moduli. The nondimensional image force $F_{20}$ versus $\kappa_3$ is depicted in Figure 5 for three values of $\rho$. It is observed that the image force versus the mismatch of piezoelectric moduli may be non-monotonic for certain combinations of shear and dielectric moduli because of the intricate coupling interaction. In this example, when $\rho = 10$, with the increase of $\kappa_3$, the dislocation is first attracted by the inclusion and the image force decreases from a limit value to zero, then the dislocation is repelled by the inclusion. After going up to a maximum value, the image force again decreases to zero, then changes its direction and trends to another limit value. When $\rho = 1$, the curve of the image force is monotonic, whereas when $\rho = 0.01$, the curve of the image force becomes again non-monotonic.

## 6.2. Coupling interaction arising from the geometry of inhomogeneous phases

Let the dislocation locate in Material 1, which is the PZT-5H piezoelectric ceramic with the properties $c_{44}^{(1)} = c_{44}^{(0)}$, $e_{15}^{(1)} = e_{15}^{(0)}$ and $\varepsilon_{11}^{(1)} = \varepsilon_{11}^{(0)}$ (refer to Equation (83)). We assume that there is a fixed mismatch of piezoelectric moduli between Material 1 and Material 2 and a variable mismatch of dielectric moduli between the inclusion and Material 2, and take $c_{44}^{(3)} = c_{44}^{(2)} = c_{44}^{(1)}$, $e_{15}^{(3)} = e_{15}^{(2)} = 2e_{15}^{(1)}$ and $\varepsilon_{11}^{(3)} = \beta_3 \varepsilon_{11}^{(2)} = \beta_3 \varepsilon_{11}^{(1)}$.

Define a parameter $\delta = (x - R_1 - h)/R_1$ to represent the nondimensional distance from a point on the $x$-axis in Material 1 to the bimaterial interface. The nondimensional image force $F_{10} = 2\pi R_1/(c_{44}^{(0)} b_w^2)F_1$ of the $x$-axis in Material 1 versus $\delta$ is depicted in Figure 6 for various values of $h/R_1$ (refer to Figure 1(a)), where the ratio constant $\beta_3 = 1.53$. It is observed that when $h/R_1 < 0.1$, the coupling interaction reverses the directions of image forces within a certain region in Material 1. As $h/R_1$ decreases, the stronger coupling interaction makes the reversion region expand. We keep $h/R_1 = 0.1$ but change $\beta_3$ representing the mismatch of dielectric moduli between the inclusion and Material 2; the nondimensional image force $F_{10}$ versus $\delta$ is depicted in Figure 7. A comparison between Figures 6 and 7 shows that the nondimensional distance $h/R_1$ has a similar effect on the image force in Material 1 with the mismatch $\beta_3$. This fact indicates that we can enhance or reduce the coupling interaction effect arising from multiple material properties by changing the geometry of inhomogeneous phases and vice versa.
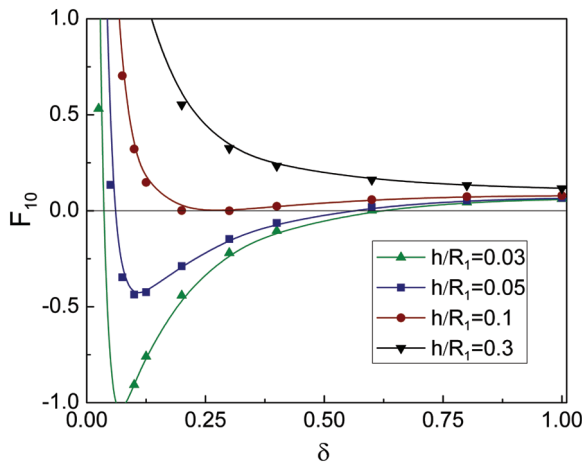
**Figure 6.** Nondimensional image force $F_{10}$ of the $x$-axis versus $\delta$ for various values of $h/R_1$, where $\varepsilon_{11}^{(3)} = \beta_3 \varepsilon_{11}^{(2)} = \beta_3 \varepsilon_{11}^{(1)}$, $c_{44}^{(3)} = c_{44}^{(2)} = c_{44}^{(1)}$, $e_{15}^{(3)} = e_{15}^{(2)} = 2e_{15}^{(1)}$ and $\beta_3 = 1.53$.

## 7. Dislocation equilibrium position

Lastly, we discuss the dislocation equilibrium position, which is of practical importance. Because of symmetry, the dislocation equilibrium point always lies on the $x$-axis (refer to Figure 1).

Consider the dislocation equilibrium point in Material 1. Apparently, if the dislocation is attracted or repelled by Material 2 and the inclusion at the same time, no equilibrium point appears. If the dislocation is attracted by one of Material 2 and the inclusion, but repelled by the other, there may be no equilibrium point, or one equilibrium point or two equilibrium points in Material 1. For example, when $h/R_1 > 0.1$ in the case of Figure 6, the repulsion by Material 2 is always larger than attraction by the inclusion and no equilibrium point in any place of Material 1 appears; when $h/R_1 = 0.1$, one unstable equilibrium point appears; when $h/R_1 < 0.1$, two equilibrium points appear. It can be found that in the latter case the left equilibrium point is stable, the right one is unstable and the direction of the image force between the two equilibrium points is reversed. It is interesting to note that the reversion region of image forces induced by the inclusion does not connect with the bimaterial interface, but has a certain distance from it. Tests showed such an interesting phenomenon. In nanoindentation tests of crystals [36,37], the dislocation nucleation first occurs at a position of certain depth from the surface, which does not connect with the surface. Figure 7 shows that the inversion of the image force is also produced by changing the property of the inclusion.

Our study shows that only one unstable dislocation equilibrium point appears in Material 2. If the dislocation is attracted or repelled by Material 1 and the inclusion at the same time, an unstable equilibrium point lies between the inclusion and the bimaterial interface (on the right of the inclusion). In other cases the unstable equilibrium point lies on the left of the inclusion.

Now consider the dislocation equilibrium point in the inclusion. In the special case that Material 1 has the same electroelastic properties as Material 2, the problem degenerates into the one of a circular piezoelectric inclusion in an infinite piezoelectric medium. The image force field in the inclusion becomes centrosymmetric and there is one equilibrium point at the center of inclusion. When the infinite piezoelectric medium attracts dislocations in the inclusion, the equilibrium point at the center is unstable; when it repels dislocations, the equilibrium point is stable.

We find that when Materials 1 and 2 have dissimilar electroelastic properties, the number and stability of the equilibrium points do not change. However, its position is away from the center and varies with mismatches of electroelastic properties in the bimaterial. As an example, we assume that the inclusion is the PZT-5H piezoelectric ceramic, that is, $c_{44}^{(3)} = c_{44}^{(0)}$, $e_{15}^{(3)} = e_{15}^{(0)}$ and $\varepsilon_{11}^{(3)} = \varepsilon_{11}^{(0)}$ (refer to Equation (83)), and take $c_{44}^{(1)} = \alpha_1 c_{44}^{(2)} = \alpha_1 c_{44}^{(3)}$, $\varepsilon_{11}^{(1)} = \varepsilon_{11}^{(2)} = \varepsilon_{11}^{(3)}$ and $e_{15}^{(1)} = e_{15}^{(2)} = 0.5 e_{15}^{(3)}$, where $\alpha_1$ refer to (85). The nondimensional image force $F_{30} = 2\pi R_1 / (c_{44}^{(0)} b_w^2) F_3$ of the $x$-axis in the inclusion versus the nondimensional coordinate $x/R_1$ for different values of $\alpha_1$ is illustrated in Figure 8, where $h/R_1 = 0.1$. It is observed that there is one unstable equilibrium point in all cases, which moves to the left as $\alpha_1 < 1$ or to the right as $\alpha_1 > 1$.
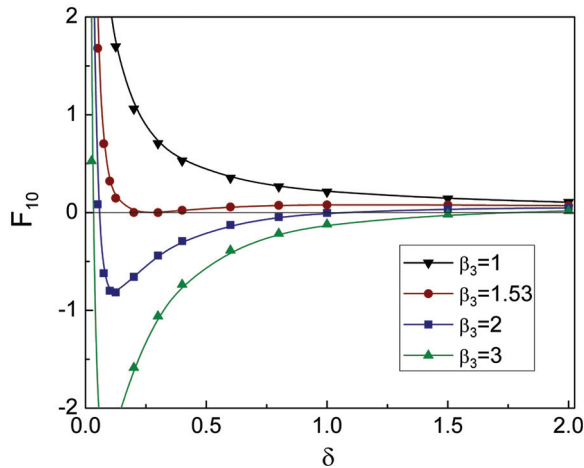
**Figure 7.** Nondimensional image force $F_{10}$ of the x-axis versus $\delta$ for various values of $\beta_3$, where $\varepsilon_{11}^{(3)} = \beta_3 \varepsilon_{11}^{(2)} = \beta_3 \varepsilon_{11}^{(1)}$, $c_{44}^{(3)} = c_{44}^{(2)} = c_{44}^{(1)}$, $e_{15}^{(3)} = e_{15}^{(2)} = 2e_{15}^{(1)}$ and $h/R_1 = 0.1$.
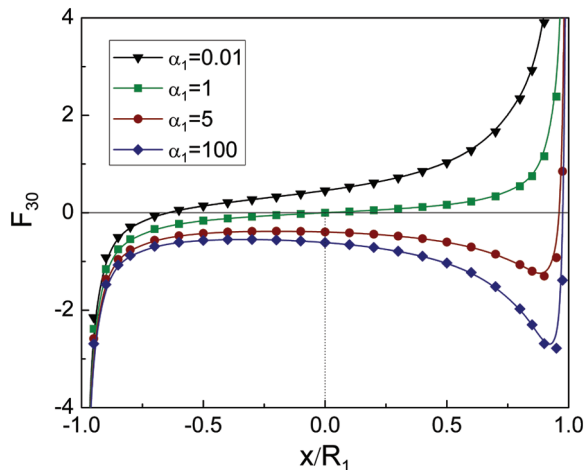


**Figure 8.** Nondimensional image force $F_{30}$ of the x-axis versus $x/R_1$ for various values of $\alpha_1$, where $c_{44}^{(1)} = \alpha_1 c_{44}^{(2)} = \alpha_1 c_{44}^{(3)}$, $\varepsilon_{11}^{(1)} = \varepsilon_{11}^{(2)} = \varepsilon_{11}^{(3)}$, $e_{15}^{(1)} = e_{15}^{(2)} = 0.5 e_{15}^{(3)}$ and $h/R_1 = 0.1$.

## 8. Conclusions

The coupling interaction of a piezoelectric screw dislocation with a bimaterial containing a circular inclusion is dealt with. Explicit series solutions are obtained by using the complex potential and the conformal mapping technique. The solutions are cast into new expressions with the coupling interaction effects separated. The new expressions converge more rapidly, and in many cases their one-order approximation formulae have satisfactory accuracy.

The present solutions can help us to understand interesting and intricate coupling interaction phenomena, which arise from multiple material properties (mechanical, piezoelectric and dielectric properties) as well as from the geometry of the inhomogeneous phases. We can enhance or reduce the coupling interaction effects arising from multiple material properties by changing the geometry of inhomogeneous phases and vice versa. It is found that when the piezoelectric moduli of three materials are zero, the shear and dielectric moduli do not yield the coupling effect, whereas when the piezoelectric moduli are not zero, the shear and dielectric moduli yield the coupling effect. The image force versus the mismatch of piezoelectric moduli may exhibit strongly nonlinear and non-monotonic relations under certain conditions.

We find that there is one dislocation equilibrium point in the inclusion, and its stability is determined by the mismatch between the inclusion and the material containing the inclusion. There is one unstable dislocation equilibrium point in the material containing the inclusion. There may be two, one or no dislocation equilibrium points in the material without any inclusion, depending on the properties and position geometry of the three materials.

## Declaration of Conflicting Interests

## Funding

## References

[1]   Bonilla, LL, and Carpio, A. Driving dislocations in grapheme. *Science* 2012; 337: 161–162.

[2]   Head, AK. The interaction of dislocations and boundaries. *Phil Mag* 1953; 44: 92–94.

[3]   Smith, E. The interaction between dislocations and inhomogeneities-I. *Int J Eng Sci* 1968; 6: 129–143.

[4]   Dundurs, J, and Mura, T. Interaction between an edge dislocation and a circular inclusion. *J Mech Phys Solids* 1964; 12: 177–189.

[5]   Sendeckyj, GP. Screw dislocations near circular inclusions. *Phys Status Solidi A* 1970; 3: 529–535.

[6]   Hirth, JP, and Lothe, J. *Theory of Dislocations*. 2nd ed. New York: John Wiley, 1982.

[7]   Gong, SX, and Meguid, SA. A screw dislocation interacting with an elastic elliptical inhomogeneity. *Int J Eng Sci* 1994; 32: 1221–122.

[8]   Xiao, ZM, and Chen, BJ. A screw dislocation interacting with a coated fiber. *Mech Mater* 2000; 32: 485–494.

[9]   Fan, H, and Wang, GF. Screw dislocation interacting with imperfect interface. *Mech Mater* 2003; 35: 943–953.

[10]  Liu, YW, Jiang, CP, and Cheung, YK. A screw dislocation interacting with an interphase layer between a circular inhomogeneity and the matrix. *Int J Eng Sci* 2003; 41: 1883–1898.

[11]  Lubarda, VA, and Markenscoff, X. The stress field for a screw dislocation near cavities and straight boundaries. *Mater Sci Eng A* 2003; 349: 327–334.

[12]  Wang, X, and Sudak, LJ. Interaction of a screw dislocation with an arbitrary shaped elastic inhomogeneity. *ASME J Appl Mech* 2006; 73: 206–211.

[13]  Shen, Y, and Anderson, PM. Transmission of a screw dislocation across a coherent, slipping interface. *Acta Mater* 2006; 54: 3941–3951.

[14]  Wu, MS, and Wang, HY. Solutions for edge dislocation in anisotropic film–substrate system by the image method. *Math Mech Solids* 2007; 12: 183–212.

[15]  Lee, CL, and Li, SF. The size effect of thin films on the Peierls stress of edge dislocations. *Math Mech Solids* 2008; 13: 316–335.

[16]  Ogbonna, N. Force on a screw dislocation in a multiphase laminated structure. *Math Mech Solids* 2014; 19: 694–702.

[17]  Li, J, Liu, YW, and Wen, PH. An edge dislocation interacting with an elastic thin-layered semi-infinite matrix. *Math Mech Solids* 2014; 19: 626–639.

[18]  Gutkin, MYu, Sheinerman, AG, and Smirnov, MA. Elastic behavior of screw dislocations in porous solids. *Mech Mater* 2009; 41: 905–918.

[19]  Ahmadzadeh-Bakhshayesh, H, Gutkin, MYu, and Shodja, HM. Surface/interface effects on elastic behavior of a screw dislocation in an eccentric core-shell nanowire. *Int J Solids Struct* 2012; 49: 1665–1675.

[20]  Jiang, CP, Chai, H, Yan, P, et al. The interaction of a screw dislocation with a circular inhomogeneity near the free surface. *Arch Appl Mech* 2014; 84: 343–353.

[21]  Pak, YE. Force on piezoelectric screw dislocation. *ASME J Appl Mech* 1990; 57: 863–869.

[22]  Liu, J, Du, S, and Wang, B. A screw dislocation interacting with a piezoelectric bimaterial interface. *Mech Res Commun* 1999; 26: 415–420.

[23]  Kattis, MA, Providas, E, and Kalamkarov, AL. Two-phase potentials in the analysis of smart composites having piezoelectric components. *Compos Part B* 1998; 29: 9–14.

[24]  Deng, W, and Meguid, SA. Analysis of a screw dislocation inside an elliptical inhomogeneity in piezoelectric solids. *Int J Solids Struct* 1999; 36: 1449–1469.

[25] Liu, JX, Jiang, ZQ, and Feng, WJ. On the electro–elastic interaction of piezoelectric screw dislocation with an elliptical inclusion in piezoelectric materials. *Appl Math Mech* 2000; 21: 1185–1190.

[26] Huang, Z, and Kuang, ZB. Dislocation inside a piezoelectric media with an elliptical inhomogeneity. *Int J Solids Struct* 2001; 38: 8459–8479.

[27] Kwon, JH, and Lee, KY. Electromechanical effects of a screw dislocation around a finite crack in a piezoelectric material. *ASME J Appl Mech* 2002; 69: 55–62.

[28] Liu, YW, Fang, QH, and Jiang, CP. A piezoelectric screw dislocation interacting with an interphase layer between a circular inclusion and the matrix. *Int J Solids Struct* 2004; 41: 3255–3274.

[29] Shen, MH, Chen, SN, and Chen, FM. A piezoelectric screw dislocation interacting with a nonuniformly coated circular inclusion. *Int J Eng Sci* 2006; 44: 1–13.

[30] Wu, XF, Cohn, S, and Dzenis, YA. Screw dislocation interacting with interfacial and interface cracks in piezoelectric biomaterials. *Int J Eng Sci* 2003; 41: 667–682.

[31] Zheng, JL, Fang, QH, and Liu, YW. A generalized screw dislocation interacting with interfacial cracks along a circular inhomogeneity in magnetoelectroelastic solids. *Theor Appl Fract Mech* 2007; 47: 205–218.

[32] Fang, QH, Feng, H, and Liu, YW. Electroelastic interaction between piezoelectric screw dislocation and circularly layered inclusion with imperfect interfaces. *Appl Math Mech* 2013; 34: 45–62.

[33] Wang, X, Pan, E, and Roy, A. Interaction between a screw dislocation and a piezoelectric circular inclusion with viscous interface. *J Mech Mater Struct* 2008; 3: 761–773.

[34] Tiersten, HF. *Linear Piezoelectric Plate Vibrations*. New York: Plenum, 1969.

[35] Muskhelishvili, NL. *Some Basic Problems of Mathematical Theory of Elasticity*. Leyden: Noordhoff, 1975.

[36] Gouldstone, A, Van Vliet, KJ, and Suresh, S. Nanoindentation simulation of defect nucleation in a crystal. *Nature* 2001; 411: 656–656.

[37] Schall, P, Cohen, I, Weitz, DA, et al. Visualizing dislocation nucleation by indenting colloidal crystals. *Nature* 2006; 440: 319–323.